

A biomimetic eye with a hemispherical perovskite nanowire array retina

<https://doi.org/10.1038/s41586-020-2285-x>

Received: 10 April 2019

Accepted: 17 March 2020

Published online: 20 May 2020

 Check for updates

Leilei Gu¹, Swapnadeep Poddar¹, Yuanjing Lin^{1,2}, Zhenghao Long¹, Daquan Zhang¹, Qianpeng Zhang¹, Lei Shu¹, Xiao Qiu¹, Matthew Kam¹, Ali Javey^{2,3} & Zhiyong Fan¹✉

Human eyes possess exceptional image-sensing characteristics such as an extremely wide field of view, high resolution and sensitivity with low aberration¹. Biomimetic eyes with such characteristics are highly desirable, especially in robotics and visual prostheses. However, the spherical shape and the retina of the biological eye pose an enormous fabrication challenge for biomimetic devices^{2,3}. Here we present an electrochemical eye with a hemispherical retina made of a high-density array of nanowires mimicking the photoreceptors on a human retina. The device design has a high degree of structural similarity to a human eye with the potential to achieve high imaging resolution when individual nanowires are electrically addressed. Additionally, we demonstrate the image-sensing function of our biomimetic device by reconstructing the optical patterns projected onto the device. This work may lead to biomimetic photosensing devices that could find use in a wide spectrum of technological applications.

Biological eyes are arguably the most important sensing organ for most of the animals on this planet. In fact, our brains acquire more than 80% of information about our surroundings via our eyes⁴. A human eye with a concavely hemispherical retina and light-management components is particularly notable for its exceptional characteristics including a wide field of view (FOV) of 150°–160°, a high resolution of 1 arcmin per line pair at the fovea and excellent adaptivity to the optical environment¹. Particularly, the domed shape of the retina has the merit of reducing the complexity of optical systems by directly compensating the aberration from the curved focal plane⁵. Mimicking human eyes, artificial vision systems are just as essential in autonomous technologies such as robotics. Particularly for humanoid robots, the vision system should resemble that of a human in appearance to enable amicable human–robot interaction, in addition to having superior device characteristics. In principle, a hemispherical image sensor design mimicking that of the human retina can achieve this goal. However, commercial charge-coupled device (CCD) and complementary-metal-oxide-semiconductor (CMOS) image sensors are mainly using planar device structures shaped by mainstream planar microfabrication processes, making hemispherical device fabrication almost impossible.

Here we demonstrate an artificial visual system using a spherical biomimetic electrochemical eye (EC-EYE) with a hemispherical retina made of a high-density perovskite nanowire array grown using a vapour-phase approach. An ionic liquid electrolyte was used as a front-side common contact to the nanowires and liquid-metal wires were used as back contacts to the nanowire photosensors, mimicking human nerve fibres behind the retina. Device characterizations show that the EC-EYE has a high responsivity, a reasonable response speed, a low detection limit and a wide FOV. The EC-EYE also demonstrates the basic function of a human eye to acquire image patterns. In addition to its structural similarity with a human eye, the hemispherical artificial

retina has a nanowire density much higher than that of photoreceptors in a human retina and can thus potentially achieve higher image resolution, which is bolstered by implementation of a single-nanowire ultrasensitive photodetector.

Figure 1 shows a comparison of the human (Fig. 1a–c) and EC-EYE imaging systems (Fig. 1d–f). The human visual system has two eye bulbs for optical sensing, millions of nerve fibres for data transmission and a brain for data processing. The human brain has enormous capability for parallel processing: neuroelectric signals from about a million nerve fibres can be processed simultaneously, enabling high-speed image processing and recognition⁶. The internal structure of a human eye (Fig. 1b) has a lens, a spherical cavity and a hemispherical retina, which is the core component required to convert optical images to neuroelectric signals. Its hemispherical shape simplifies optical design, resulting in an extraordinarily large FOV of about 155° with a wide visual perception of the surroundings¹. There are about 100–120 million photoreceptors and rod and cone cells, vertically assembled in the retina in a dense and quasi-hexangular manner (Fig. 1c), with a density of around 10 million per square centimetre and an average pitch of 3 μm, leading to a high imaging resolution comparable to that of the state-of-the-art CCD/CMOS sensors⁷. However, the nerve fibre layer is at the front surface of the human retina, causing light loss and blind spot issues (Supplementary Fig. 1)¹. Figure 1d, e illustrates the schematic of our biomimetic visual system, which consists of a lens, a photosensor array on a hemispherical substrate and thin liquid-metal wires as electrical contacts. These components mimic the biological eye's lens, retina and the nerve fibres behind the retina, respectively. Of these, the key component is the artificial retina made of a high-density array of perovskite nanowires grown inside a hemispherical porous aluminium oxide membrane (PAM) via a vapour-phase deposition process^{8–10}.

¹Department of Electronic and Computer Engineering, The Hong Kong University of Science and Technology, Kowloon, Hong Kong SAR, China. ²Electrical Engineering and Computer Sciences, University of California, Berkeley, CA, USA. ³Materials Sciences Division, Lawrence Berkeley National Laboratory, Berkeley, CA, USA. ✉e-mail: eezfan@ust.hk

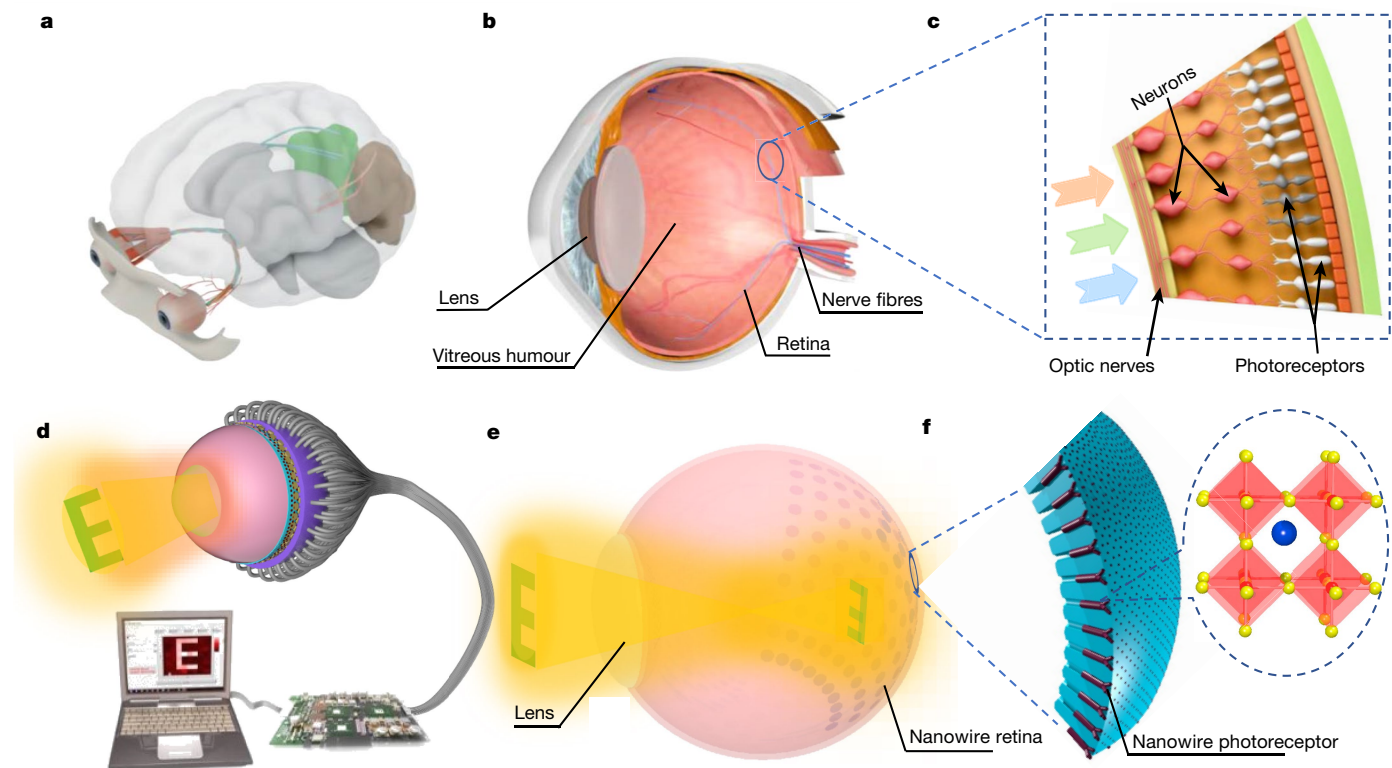


Fig. 1 | Overall comparison of the human visual system and the EC-EYE imaging system. a–c, Schematic of the human visual system (a), the human eye (b) and the retina (c). **d–f,** Schematic of our EC-EYE imaging system (d), the

working mechanism of EC-EYE (e) and perovskite nanowires in the PAM template and their crystal structure (f).

A more detailed structure of the EC-EYE is in Fig. 2a, and the fabrication process is in Methods and Supplementary Fig. 2. The nanowires serve as light-sensitive working electrodes. The tungsten (W) film on aluminium (Al) hemispherical shell works as the counter electrode. In between two electrodes, ionic liquid is used to fill the cavity, serving as the electrolyte and mimicking the vitreous humour in the human eye. The flexible eutectic gallium indium liquid-metal wires in soft rubber tubes are used for signal transmission between the nanowires and external circuitry with a discontinuous indium layer between the liquid metal and the nanowires to improve contact (Supplementary Fig. 3). An individual photodetector can be addressed and measured by selecting the corresponding liquid-metal wire. This resembles the working principle of the human retina, in which groups of photoreceptors are individually connected with nerve fibres¹¹, enabling suppressed interference among pixels and high-speed parallel processing of the neuroelectric signals. We note that the liquid-metal wires are behind the sensing material, thus avoiding the light-loss and blind-spot problems of the human retina. As a proof of concept, we fabricated a 10×10 photodetector array with a pitch of 1.6 mm. The minimum size of each sensing pixel is limited by the diameter of the liquid-metal wire, which is difficult to reduce to a few micrometres¹². To further reduce pixel size and enhance the spatial imaging resolution, another approach to fabricating the sensor pixel array with a pixel area of about $1 \mu\text{m}^2$ per pixel using metal microneedles has been developed.

Previously, there have been a few inspiring works reporting hemispherical image sensors using deformed, folded or individually assembled photodetectors^{13–15}. The photodetectors in those works were mainly pre-fabricated on planar substrates, then transferred to a hemispherical supporting material or folded into a hemispherical shape. It is challenging to achieve small individual pixel size and high imaging resolution owing to the complexity of the fabrication process. Here light-sensing nanowires were grown in a hemispherical template, and

thus a structure akin to that of the human retina has been formed in a single step. We chose formamidinium lead iodide (FAPbI₃) as the model material for nanowire growth here owing to its excellent optoelectronic properties and decent stability^{9,16}. The nanowire growth and characterization details can be found in Methods and Supplementary Figs. 4 and 5. In principle, other types of inorganic nanowires made of Si, Ge, GaAs and so on can also be grown using the well documented vapour–liquid–solid process^{17–20}. Figure 2b, c shows the side and top views of a completed EC-EYE. Figure 2d, e presents scanning electron microscopy (SEM) images of the hemispherical PAM and the nanowires located at the bottom of the nanochannels, respectively. The single-crystalline (Fig. 2f) nanowires have a pitch of 500 nm, corresponding to a density of $4.6 \times 10^8 \text{ cm}^{-2}$, which is much higher than that of the photoreceptors in human retina, indicating the potential to achieve a high imaging resolution if proper electrical contacts can be achieved²¹.

Figure 3a shows the schematic of a single pixel measurement. A collimated light beam is focused on the pixels at the centre of the retina. Figure 3b plots the energy-band alignment for the entire device showing charge-carrier separation routes under light excitation. Figure 3c presents the current–voltage characteristics exhibiting the asymmetric photoresponse caused by asymmetric charge transportation at the two sides of the nanowires (Fig. 3b). Previous electrochemical characterizations have shown that the redox reactions of I^-/I_3^- pairs^{22,23} occur at the nanowire/electrolyte and tungsten film/electrolyte interfaces and that ion transportation inside the electrolyte contributes to the photoresponse (Supplementary Fig. 6). The inset of Fig. 3c shows the transient response of the device to chopped light (see Supplementary Figs. 7 and 8 for more results). The relatively fast and highly repeatable response indicates that the device has excellent photocurrent stability and reproducibility. The response and recovery time are found to be 32.0 ms and 40.8 ms, respectively. Further electrochemical analysis of the critical nanowire/electrolyte interface reveals that the device

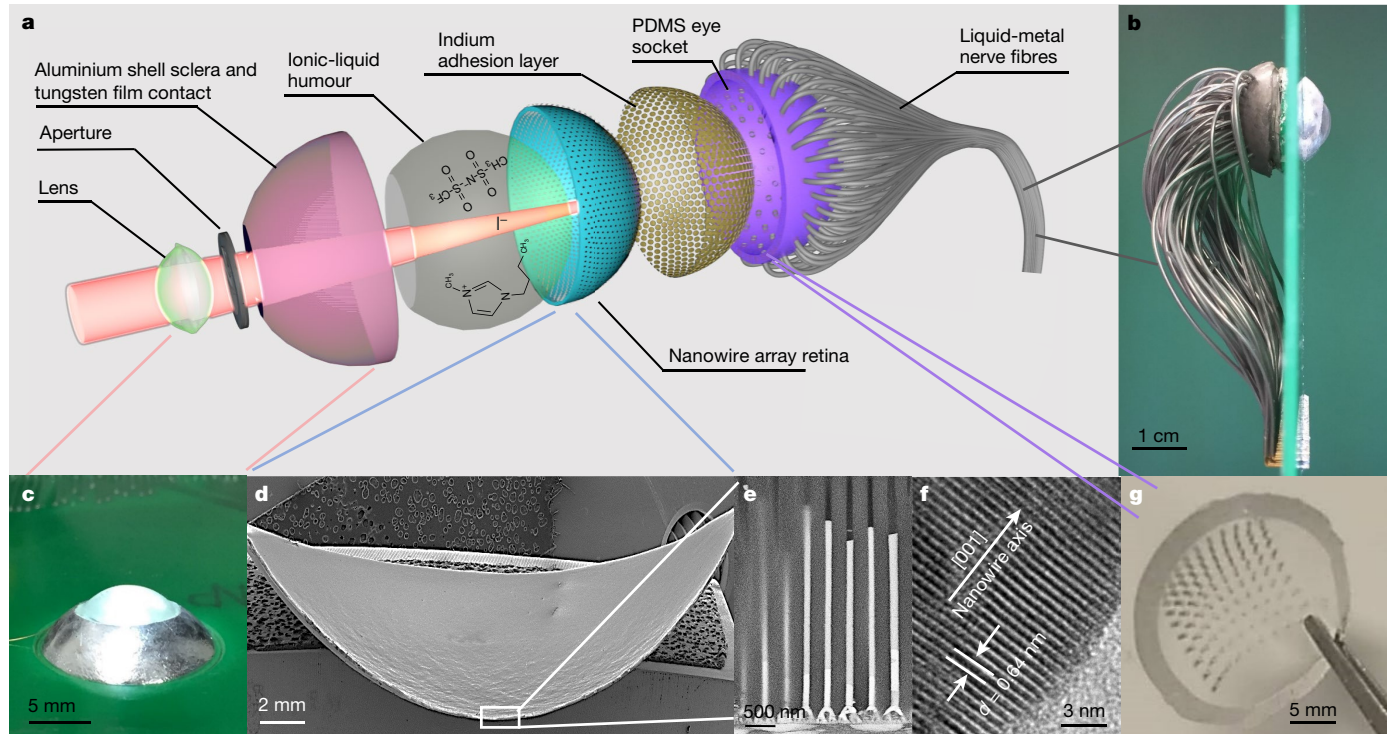


Fig. 2 | Detailed structure of our EC-EYE. **a**, Exploded view of EC-EYE. **b, c**, Side view (**b**) and top view (**c**) of a completed EC-EYE. **d**, Low-resolution cross-sectional SEM image of the hemispherical PAM/nanowires. **e**, Cross-sectional SEM images of nanowires in PAM. **f**, High-resolution transmission electron microscopy image of a single-crystalline perovskite nanowire. **g**, Photograph of the polydimethylsiloxane (PDMS) socket, which improves the alignment of the liquid-metal wires.

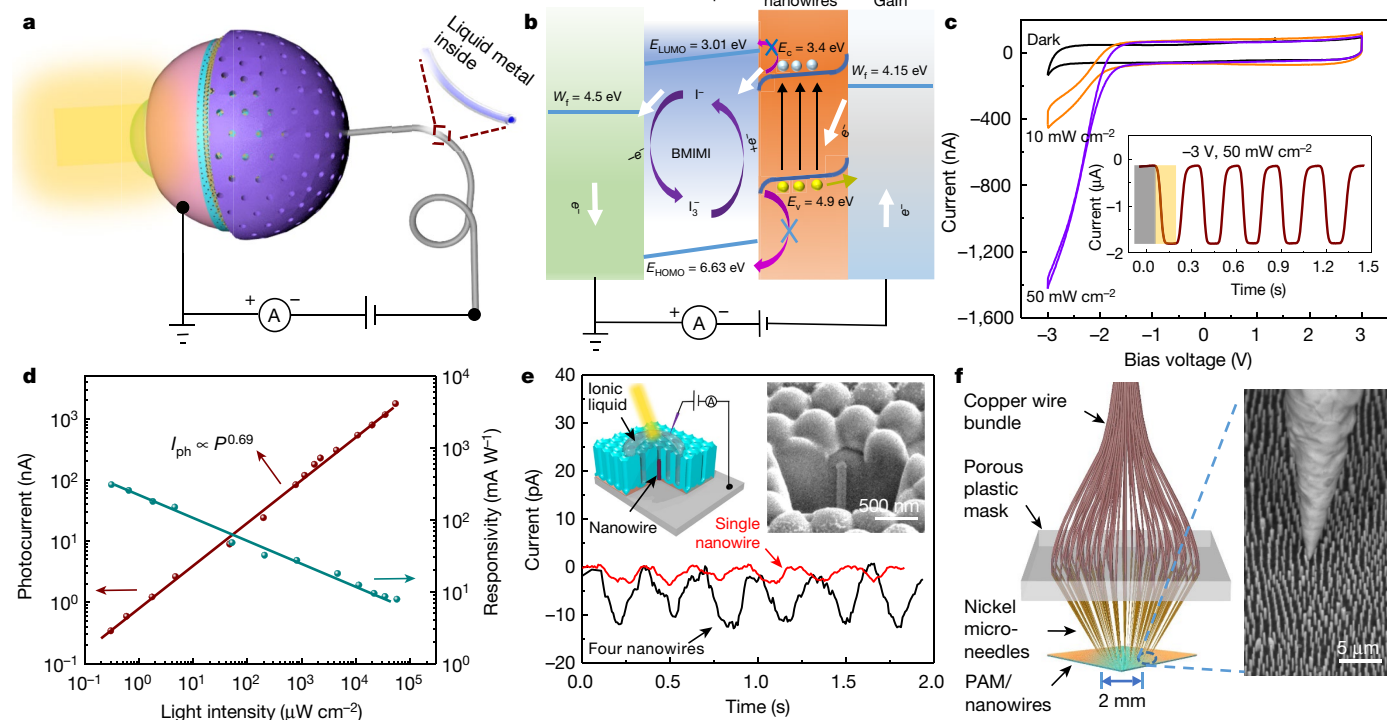


Fig. 3 | Photodetection performance characterization of individual pixels. **a**, Schematic setup of individual pixel measurement. **b**, Working mechanism of an individual pixel under -3 V bias voltage. BMIMI, 1-butyl-3-methylimidazolium iodide. **c**, Current-voltage curves under different illuminations and the transient response of individual pixels under the illumination of simulated sunlight with an intensity of 50 mW cm^{-2} . The current-voltage curves represent one cycle of the cyclic-voltammetry measurement. Scan rate, 100 mV s^{-1} . **d**, Illumination-intensity-dependent photocurrent and responsivity of an individual pixel. The lowest light intensity is $0.3 \mu\text{W cm}^{-2}$. **e**, Device schematic and transient photoresponse of single-nanowire-based and four-nanowire-based individual pixels. **f**, Schematic and SEM image of the Ni microneedle contact to the nanowire array.

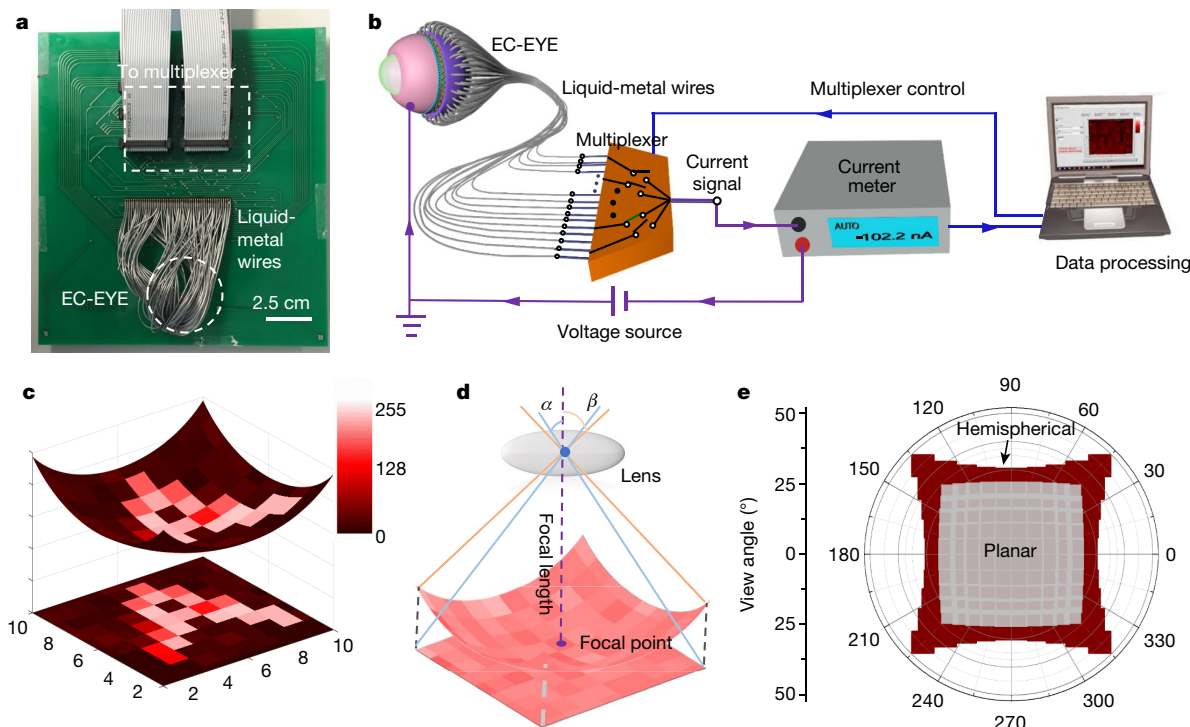


Fig. 4 | Image-sensing demonstration of EC-EYE. a, Back-view photo of an EC-EYE mounted on a printed circuit board. **b**, Schematic illustration of the measurement setup. **c**, The reconstructed image (letter 'A') of EC-EYE and its

projection on a flat plane. **d, e**, The schematic (**d**) and calculated (**e**) FOV of the planar and hemispherical image-sensing systems.

response time depends on the kinetics of multiple types of ions at that interface (Supplementary Fig. 9). Electrochemical impedance spectroscopy measurements (Supplementary Fig. 10) demonstrate that device structural optimization and ionic liquid concentration increase can substantially reduce the charge-transfer resistance (R_{ct}) at the nanowire/electrolyte interface, leading to reduction of the device response and recovery times to 19.2 ms and 23.9 ms. This is much faster than that of human eyes, whose response and recovery times range from 40 ms to 150 ms (ref. 24). Meanwhile, increasing ionic liquid concentration leads to light absorption loss (Supplementary Fig. 11), so further optimization of the ionic liquid composition will be of benefit.

Figure 3d shows the dependence of the photocurrent and responsivity on the illumination intensity, with a large dynamic range from $0.3 \mu\text{W cm}^{-2}$ to 50 mW cm^{-2} . The photocurrent can be fitted with a quasi-linear power-law relationship ($I = A \times P^{0.69}$), where I is the photocurrent, P represents the irradiance power and A is a coefficient. Intriguingly, the responsivity increases when reducing illumination intensity. It can reach up to 303.2 mA W^{-1} , which is among the highest for reported photoelectrochemical photodetectors (Supplementary Table 1). And it is on par with that of the solid-state photodetectors based on perovskite nanowire arrays reported earlier^{8,9}. Under the lowest radiation level measured, the average number of photons received per second by an individual nanowire can be estimated at 86 photons (Supplementary Information). This sensitivity is on par with that of human cone cells²⁵. The corresponding specific detectivity is calculated as about 1.1×10^9 Jones for $0.3 \mu\text{W cm}^{-2}$ incident light. The spectral responsivity shows a broad-band response with a clear cut-off at 810 nm (Supplementary Fig. 12). Supplementary Fig. 13 demonstrates the stability and repeatability of an individual pixel for 2 Hz light continuously chopped for 9 h. It indicates that although there are drifts for both the dark and light current, there is no obvious device performance degradation after 64,800 cycles.

As mentioned, one of the primary merits of using high-density nanowire arrays for artificial retina is their potential for high image

resolution. Although liquid-metal fibre contacts to nanowires are convenient and image resolution is already on par with that of a number of existing bionic eyes in use^{26–28}, it is challenging to reduce pixel size down to the few-micrometres level. Therefore, we explored two more contact strategies to achieve ultrasmall pixel size. As shown in Fig. 3e, a single nanowire was deterministically grown in a single nanochannel opened using a focused ion beam; then a single pixel with 500-nm lateral size and a footprint of about $0.22 \mu\text{m}^2$ was achieved (Methods and Supplementary Fig. 14). Using the same approach, a pixel of 4 nanowires was also fabricated. The SEM images in Supplementary Fig. 15 show the controllable growth of nanowires, including the nanowire numbers and positions. The photoresponses of these two devices are shown in Fig. 3e. To form an array of ultrasmall pixels, nickel (Ni) microneedles were vertically assembled on top of a PAM using a magnetic field and thus each microneedle can address 3 nanowires, forming a pixel with lateral size of about $1 \mu\text{m}$ and pitch of $200 \mu\text{m}$. The details of this contact strategy are illustrated in Supplementary Figs. 16 and 17. Figure 3f schematically shows the device connected to copper wires, which serve as signal transmission lines. The lateral size of the contact region is 2 mm.

After characterization of individual sensor pixels, we measured the full device imaging functionality. A photograph of the device is shown in Fig. 4a and Supplementary Fig. 18a, b. The liquid-metal wires are connected to a computer-controlled 100×1 multiplexer via a printed circuit board. The measurement system design is shown in Fig. 4b and the corresponding circuit diagram is shown in Supplementary Fig. 18c. The image-sensing function was examined by projecting optical patterns onto the EC-EYE, after which the photocurrent of each sensor pixel was recorded. Before pattern generation and recognition, the consistency of the dark and light currents of all pixels was verified. Supplementary Fig. 19a, b depicts the dark- and light-current images obtained under -3 V bias voltage, showing that all 100 pixels have consistent photoresponse with relatively small variation. To reconstruct the optical pattern projected on the EC-EYE, a photocurrent value was converted to a greyscale number between 0 and 255 (Supplementary Information).

Figure 4c shows the imaged character 'A' and its projection onto a flat plane. Supplementary Fig. 20 shows images of letters 'E', 'I' and 'Y'. The Supplementary Video shows the dynamic process of EC-EYE capturing the letters 'E', 'Y' and 'E' sequentially. Compared to planar image sensors based on a crossbar structure, the device presented here delivers a higher contrast with clearer edges because each individual pixel is better isolated from the neighbouring pixels (Supplementary Fig. 21). Besides an EC-EYE with liquid-metal contacts, we also fabricated a small electrochemical image sensor with microneedle contacts. This imager, with an active area of 2 mm × 2 mm, was assembled into a mini-camera together with other optical parts (see Supplementary Figs. 22 and 23). Supplementary Fig. 23 shows its imaging functionality. Meanwhile, the magnetic microneedle alignment strategy developed here also works very well for the whole hemispherical surface. Supplementary Fig. 24 shows that the 50-µm-thick Ni microwires are well aligned onto the surface of a hemispherical PAM. Although we have successfully fabricated ultras-small pixels here and implemented microneedle manual alignment onto the nanowires, better high-throughput strategies to align large numbers of electrodes on nanowires with precision could be developed. For instance, a high-precision robotic arm equipped with a piezo actuator can be used to place Ni microneedles onto the hemispherical PAM, assisted by a magnetic field and a high-resolution optical monitoring system (Supplementary Fig. 24c). Better approaches could address individual nanowires in a more deterministic manner.

Compared to a planar image sensor, the hemispherical shape of our EC-EYE ensures a more consistent distance between pixels and the lens, resulting in a wider FOV and better focusing onto each pixels (Fig. 4d). The diagonal visual field of our hemispherical EC-EYE is about 100.1°, whereas that of a planar device is only 69.8° (Fig. 4e). Moreover, this angle of view can be further improved to approach the static vertical FOV of a single human eye (about 130°)²⁹, by optimizing the pixel distribution on the hemispherical retina.

Here we have demonstrated a biomimetic eye with a hemispherical retina made of high-density light-sensitive nanowires. Its structure has a high degree of similarity to that of a human eye with potential to achieve higher imaging resolution if a better contact strategy can be implemented. The processes developed tackle the challenge of fabricating optoelectronic devices on non-planar substrates with high integration density. Furthermore, this work may inspire biomimetic designs of optical imaging devices that could find application in scientific instrumentation, consumer electronics and robotics.

Online content

Any methods, additional references, Nature Research reporting summaries, source data, extended data, supplementary information, acknowledgements, peer review information; details of author contributions and competing interests; and statements of data and code availability are available at <https://doi.org/10.1038/s41586-020-2285-x>.

- Atchison, D. A. & Smith, G. *Optics of the Human Eye* Vol. 35 (Butterworth-Heinemann, 2000).
- Zhang, J., Con, C. & Cui, B. Electron beam lithography on irregular surfaces using an evaporated resist. *ACS Nano* **8**, 3483–3489 (2014).
- Qin, D., Xia, Y. & Whitesides, G. M. Soft lithography for micro- and nanoscale patterning. *Nat. Protocols* **5**, 491–502 (2010).
- Poock, D. C. D. Sight and knowledge. *Trans. Inst. Br. Geogr.* **6**, 385–393 (1981).
- Jung, I. et al. Dynamically tunable hemispherical electronic eye camera system with adjustable zoom capability. *Proc. Natl Acad. Sci. USA* **108**, 1788–1793 (2011).
- Nassi, J. J. & Callaway, E. M. Parallel processing strategies of the primate visual system. *Nat. Rev. Neurosci.* **10**, 360–372 (2009).
- Jonas, J. B., Schneider, U. & Naumann, G. O. Count and density of human retinal photoreceptors. *Graefes Arch. Clin. Exp. Ophthalmol.* **230**, 505–510 (1992).
- Gu, L. et al. 3D arrays of 1024-pixel image sensors based on lead halide perovskite nanowires. *Adv. Mater.* **28**, 9713–9721 (2016).
- Gu, L. et al. Significantly improved black phase stability of FAPbI₃ nanowires via spatially confined vapor phase growth in nanoporous templates. *Nanoscale* **10**, 15164–15172 (2018).
- Waleed, A. et al. Lead-free perovskite nanowire array photodetectors with drastically improved stability in nanoengineering templates. *Nano Lett.* **17**, 523–530 (2017).
- Schein, S. J. Anatomy of macaque fovea and spatial densities of neurons in foveal representation. *J. Comp. Neurol.* **269**, 479–505 (1988).
- Dickey, M. D. et al. Eutectic gallium-indium (EGaIn): a liquid metal alloy for the formation of stable structures in microchannels at room temperature. *Adv. Funct. Mater.* **18**, 1097–1104 (2008).
- Song, Y. M. et al. Digital cameras with designs inspired by the arthropod eye. *Nature* **497**, 95–99 (2013).
- Ko, H. C., Stoykovich, M. P., Song, J., Malyarchuk, V. & Rogers, J. A. A hemispherical electronic eye camera based on compressible silicon optoelectronics. *Nature* **454**, 748–753 (2008).
- Zhang, K. et al. Origami silicon optoelectronics for hemispherical electronic eye systems. *Nat. Commun.* **8**, 1782 (2017).
- Han, Q. et al. Single crystal formamidinium lead iodide (FAPbI₃): insight into the structural, optical, and electrical properties. *Adv. Mater.* **28**, 2253–2258 (2016).
- Fan, Z. et al. Ordered arrays of dual-diameter nanopillars for maximized optical absorption. *Nano Lett.* **10**, 3823–3827 (2010).
- Fan, Z. et al. Three-dimensional nanopillar-array photovoltaics on low-cost and flexible substrates. *Nat. Mater.* **8**, 648–653 (2009).
- Ramdani, M. R. et al. Fast growth synthesis of GaAs nanowires with exceptional length. *Nano Lett.* **10**, 1836–1841 (2010).
- Wen, C. Y. et al. Formation of compositionally abrupt axial heterojunctions in silicon-germanium nanowires. *Science* **326**, 1247–1250 (2009).
- Wandell, B. A. *Foundations of Vision* Vol. 8 (Sinauer Associates, 1995).
- Boschloo, G. & Hagfeldt, A. Characteristics of the iodide/triiodide redox mediator in dye-sensitized solar cells. *Acc. Chem. Res.* **42**, 1819–1826 (2009).
- Kawano, R. & Watanabe, M. Equilibrium potentials and charge transport of an I⁻/I₃⁻ redox couple in an ionic liquid. *Chem. Commun.* **3**, 330–331 (2003).
- Rayner, K., Smith, T. J., Malcolm, G. L. & Henderson, J. M. Eye movements and visual encoding during scene perception. *Psychol. Sci.* **20**, 6–10 (2009).
- Mustafi, D., Engel, A. H. & Palczewski, K. Structure of cone photoreceptors. *Prog. Retin. Eye Res.* **28**, 289–302 (2009).
- Fujikado, T. et al. Evaluation of phosphenes elicited by extraocular stimulation in normals and by suprachoroidal-transretinal stimulation in patients with retinitis pigmentosa. *Graefes Arch. Clin. Exp. Ophthalmol.* **245**, 1411–1419 (2007).
- Ayton, L. N. et al. First-in-human trial of a novel suprachoroidal retinal prosthesis. *PLoS One* **9**, e115239 (2014).
- Shivdasani, M. N. et al. Factors affecting perceptual thresholds in a suprachoroidal retinal prosthesis. *Invest. Ophthalmol. Vis. Sci.* **55**, 6467–6481 (2014).
- Navarro, R. The optical design of the human eye: a critical review. *J. Optom.* **2**, 3–18 (2009).

Publisher's note Springer Nature remains neutral with regard to jurisdictional claims in published maps and institutional affiliations.

© The Author(s), under exclusive licence to Springer Nature Limited 2020

Methods

Fabrication of EC-EYE

The EC-EYE fabrication process started with deforming a 500- μm -thick Al sheet on a set of hemispherical moulds to obtain a hemispherical Al shell, which then underwent a standard two-step anodization process to form PAM with thickness 40 μm and nanochannel pitch and diameter of 500 nm and 120 nm, respectively, on the Al surface. A barrier thinning process and Pb electrodeposition were carried out to obtain Pb nanoclusters at the bottom of the PAM channels. Next, the outer layer of PAM and the residual Al were etched away to obtain a freestanding PAM with Pb, which was then transferred into a tubular furnace to grow perovskite nanowires about 5 μm long. The detailed nanowire growth condition can be found in ref.⁹. A 20-nm-thick indium layer was evaporated onto the PAM back surface to serve as the adhesion layer. We note that this indium layer will not cause short-circuiting between pixels owing to its discontinuous morphology (Supplementary Fig. 3). To obtain the liquid-metal contact array, a hedgehog-shaped mould was fabricated using 3D printing, from which a complementary PDMS socket with 10×10 hole array (hole size 700 μm , pitch 1.6 mm) was cast. Eutectic gallium indium liquid metal was then injected into thin soft tubes (inner diameter 400 μm , outer diameter 700 μm) to form liquid-metal wires. Then 100 tubes were inserted into the holes on the PDMS socket and the whole socket was attached to the PAM/nanowire surface to form a 10×10 photodetector array. These long soft tubes can be directly connected to a printed circuit board and thus the complex wire bonding process is avoided. A circular hole was opened on another Al shell, which was then coated with a tungsten film working as the counter electrode of the EC-EYE. After mounting the aperture (Eakins, SK6), the Al shell was subsequently fixed onto the front side of PAM by epoxy. Ionic liquid 1-butyl-3-methylimidazolium bis(trifluoromethylsulfonyl)imide (BMIMTFSI) mixed with 1 vol% 1-butyl-3-methylimidazolium iodide (BMIMI) was then injected and a convex lens (diameter 1.2 cm, focal length 1.6 cm) was then glued to the hole on Al shell to seal the device. After curing, the EC-EYE device fabrication was completed.

Fabrication of microneedle-based electrochemical image sensor

Freestanding 40- μm -thick PAM was fabricated using the standard anodization process, NaOH etching and HgCl_2 solution etching. Ion milling was used to remove the barrier layer to achieve through-hole PAM (Supplementary Fig. 17a). Then a 1- μm -thick Cu film was thermally evaporated onto the through-hole PAM to serve as the electrode for the subsequent Ni and Pb electrochemical deposition (Supplementary Fig. 17b). Next, to expose the Ni nanowires, the copper layer was removed by Ar^+ ion milling and the PAM was partially etched away by reactive ion etching. The exposed Ni nanowires were about 3 μm long (Supplementary Fig. 17c). The chip was moved into a tubular furnace for perovskite nanowire growth (Supplementary Fig. 17c). The PAM chip was fixed onto a cylindrical electromagnet (0–50 mT) with Ni nanowires facing upward (Supplementary Fig. 17d). Meanwhile, Ni microwires of diameter 50 μm were sharpened in a mixed acidic solution (100 ml 0.25 M HCl aqueous solution + 100 ml ethylene glycol) under a bias of 1 V, with Ni microwires as the working electrodes and the tungsten coil as the counter electrode. The resulting Ni microwires have sharp tips, with curvature radius of 100–200 nm. The Ni needle was then gently placed onto the PAM substrate with the magnetic field 'on'. Owing to the magnetic force, the ferromagnetic Ni microneedles can engage into the Ni nanowire forest to form an effective electrical contact to the nanowires (Supplementary Fig. 17d). To facilitate the Ni microwire placement, a mask with 10×10 hole array (hole diameter 100 μm , pitch 200 μm) was used to align the Ni microneedles (Supplementary Fig. 17d). After placement, ultraviolet epoxy was dropped between the mask and the PAM substrate. Copper enamelled wire with diameter of 60 μm was inserted into the hole to form an electrical contact bridging the Ni microneedle and external printed circuit board (Supplementary Fig. 17e).

Fabrication of single- and multiple-nanowire-based electrochemical photodetectors

Freestanding planar PAM was fabricated by standard two-step anodization followed by HgCl_2 etching. The freestanding PAM was then transferred into the focused ion beam (FEI Helios G4 UX) to selectively etch away the barrier layer (Supplementary Fig. 14c). To facilitate the etching, the chip was bonded onto an Al substrate with the barrier layer side facing up. After focused-ion-beam etching (etching voltage 30 kV, etching current 26 nA), a 500-nm-thick Cu layer was evaporated onto the barrier layer side to serve as the electrode for the subsequent Pb electrochemical deposition (Supplementary Fig. 14d). Next, the chip was moved into a tubular furnace for perovskite nanowire growth (Supplementary Fig. 14e). Then a Cu wire was bonded onto the Cu side of PAM with carbon paste and the whole chip was fixed onto a glass substrate by ultraviolet epoxy. After curing, ionic liquid was dropped onto the top of the PAM (Supplementary Fig. 14e) and a tungsten probe was inserted into the ionic liquid for photoelectric measurement. The photoresponse was measured with -3 V bias and 50 mW cm^{-2} light intensity.

Material and photodetector characterization

The SEM images and energy dispersive X-ray mapping of the PAM were characterized using a field-emission scanning electron microscope (JEOL JSM-7100F equipped with a Si (Li) detector and PGT 4000T analyser). The X-ray diffraction patterns of the FAPbI_3 nanowire arrays in PAM were obtained using a Bruker D8 X-ray diffractometer. Transmission electron microscope images were obtained using a TEM JEOL (2010) with 200-kV acceleration voltage. The ultraviolet–visible absorption was measured with a Varian Cary 500 spectrometer. The photoluminescence and time-resolved photoluminescence measurements were carried out on an Edinburgh FS5 fluorescence spectrometer. The cyclic-voltammetry measurements based on a two-electrode configuration were performed on an electrochemical workstation (CHI 660E, China) at a scan rate of 100 mV s^{-1} with attenuated simulated sunlight (Newport, Solar Spectral Irradiance Air Mass 1.5) as the light source. The current–time curves of individual pixels were measured using the probe station of a HP4156A with neutral-density filters to tune the light intensity. An additional chopper was used to chop light into square wave optical signals with different frequencies. The electrochemical impedance spectra were measured by a potentiostat (Gamry SG 300) in the range 300 kHz to 100 Hz, with an amplitude of 10 mV under a bias of -3 V. The working electrodes were connected to the liquid metal. The reference and counter electrodes were connected to the tungsten electrode.

Image-sensing characterization of EC-EYE

The image-sensing performance of EC-EYE was characterized by using a home-built system consisting of a multiplexer, a pre-amplifier, a laptop computer and a Labview program (<https://www.ni.com/zh-cn/shop/labview.html>). The schematic of the system can be found in Fig. 4b. Specifically, Keithley 2400 was used to provide the bias voltage. The current meter (PXI4130, National Instruments), together with the multiplexer (PXI2530B, National Instruments), was installed inside of a chassis (PXI1031, National Instruments). The whole system is controlled by a home-built Labview program. To carry out the measurements, various optical patterns were generated by PowerPoint slides and projected onto the device by a projector. A convex lens was used to focus the pattern and different neutral-density filters were inserted between the projector and image sensor to tune the light intensity.

Reporting summary

Further information on research design is available in the Nature Research Reporting Summary linked to this paper.

Data availability

The data that support the findings of this study are provided in the main text and the Supplementary Information. More data are available from the corresponding author upon reasonable request.

Acknowledgements This work was supported by the National Natural Science Foundation of China (project 51672231) and the Science and Technology Plan of Shenzhen (JCYJ20170818114107730), the General Research Fund (projects 16237816, 16309018 and 16214619) from the Hong Kong Research Grant Council, Hong Kong Innovation Technology Commission (project ITS/115/18) and The Hong Kong University of Science and Technology (HKUST) Fund of Nanhai (grant number FSNH-18FYTR101). We acknowledge support received from the Material Characterization and Preparation Facility (MCPF, particularly Y. Cai for her technical assistance with the focused ion beam), the Nanosystem Fabrication Facility (NFF), the Center for 1D/2D Quantum Materials and the State Key Laboratory on Advanced Displays and Optoelectronics at HKUST. We also thank D. Wang (Chemistry Department, Boston College), M. Shao (Department of Chemical and Biological Engineering, HKUST) and Q. Chen (Department of Mechanical and Aerospace Engineering, HKUST) for their discussions on the

electrochemical impedance spectroscopy measurements. The images in Fig. 1a–d and Supplementary Fig. 1 were created by Fantastic Color Animation Technology Co., Ltd (2020).

Author contributions Z.F. and L.G. conceived the ideas of the work. L.G., Z.L., D.Z., Q.Z. and L.S. contributed to PAM fabrication, perovskite and Ni nanowire growth. S.P. contributed to the focused-ion-beam process. Y.L. developed the photoelectrochemical working mechanism. L.G., Z.L. and X.Q. worked on Ni microneedle assembly and EC-EYE device characterizations. L.G., Y.L., M.K., A.J. and Z.F. carried out the data analysis and wrote the manuscript. All authors discussed the results and commented on the manuscript.

Competing interests The authors declare no competing interests.

Additional information

Supplementary information is available for this paper at <https://doi.org/10.1038/s41586-020-2285-x>.

Correspondence and requests for materials should be addressed to Z.F.

Peer review information *Nature* thanks Dae-Hyeong Kim, Hongrui Jiang and the other, anonymous, reviewer(s) for their contribution to the peer review of this work.

Reprints and permissions information is available at <http://www.nature.com/reprints>.